Monthly Notices
of the
ROYAL ASTRONOMICAL SOCIETY

MNRAS **488,** 3783–3793 (2019)
Advance Access publication 2019 July 25

doi:10.1093/mnras/stz1928

The Type II superluminous SN 2008es at late times: near-infrared excess and circumstellar interaction

Kornpob Bhirombhakdi [1]★ Ryan Chornock,[1] Adam A. Miller [2,3]
Alexei V. Filippenko,[4,5] S. Bradley Cenko[6,7] and Nathan Smith[8]

[1]*Astrophysical Institute, Department of Physics and Astronomy, 251B Clippinger Lab, Ohio University, Athens, OH 45701, USA*
[2]*Center for Interdisciplinary Exploration and Research in Astrophysics (CIERA), Department of Physics and Astronomy, Northwestern University, 2145 Sheridan Road, Evanston, IL 60208, USA*
[3]*The Adler Planetarium, Chicago, IL 60605, USA*
[4]*Department of Astronomy, University of California, Berkeley, CA 94720, USA*
[5]*Miller Senior Fellow, Miller Institute for Basic Research in Science, University of California, Berkeley, CA 94720, USA*
[6]*Astrophysics Science Division, NASA Goddard Space Flight Center, Mail Code 661, Greenbelt, MD 20771, USA*
[7]*Joint Space-Science Institute, University of Maryland, College Park, MD 20742, USA*
[8]*Steward Observatory, University of Arizona, 933 N. Cherry Ave., Tucson, AZ 85721, USA*

Accepted 2019 June 30. Received 2019 June 29; in original form 2018 July 20

ABSTRACT

SN 2008es is one of the rare cases of a Type II superluminous supernova (SLSN), showing no narrow features in its early-time spectra, and therefore, its powering mechanism is under debate between circumstellar interaction (CSI) and magnetar spin-down. Late-time data are required for better constraints. We present optical and near-infrared (NIR) photometry obtained from Gemini, Keck, and Palomar Observatories from 192 to 554 d after explosion. Only broad H α emission is detected in a Gemini spectrum at 288 d. The line profile exhibits red-wing attenuation relative to the early-time spectrum. In addition to the cooling SN photosphere, an NIR excess with blackbody temperature $\sim$1500 K and radius $\sim 10^{16}$ cm is observed. This evidence supports dust condensation in the cool dense shell being responsible for the spectral evolution and NIR excess. We favour CSI, with $\sim$2–3 $M_\odot$ of circumstellar material (CSM) and $\sim$10–20 $M_\odot$ of ejecta, as the powering mechanism, which still dominates at our late-time epochs. Both models of uniform density and steady wind fit the data equally well, with an effective CSM radius $\sim 10^{15}$ cm, supporting the efficient conversion of shock energy to radiation by CSI. A low amount ($\lesssim$0.4 $M_\odot$) of ^{56}Ni is possible but cannot be verified yet, since the light curve is dominated by CSI. The magnetar spin-down powering mechanism cannot be ruled out, but is less favoured because it overpredicts the late-time fluxes and may be inconsistent with the presence of dust.

Key words: circumstellar matter – supernovae: individual (SN 2008es).

1 INTRODUCTION

Superluminous supernovae (SLSNe), which are 10–100 times brighter at peak luminosity than typical SNe (e.g. Gal-Yam 2012), have been discovered recently. Analogous to normal SNe (e.g. Filippenko 1997), SLSNe are classified as Type I for H-poor or Type II for H-rich. For Type II, SLSNe are subclassified into common cases of Type II with relatively narrow features (e.g. SN 2006gy; Ofek et al. 2007; Smith et al. 2007), and uncommon cases of Type II lacking such features (e.g. SN 2008es, SN 2013hx, and PS15br; Gezari et al. 2009; Miller et al. 2009; Inserra et al. 2018).

The powering mechanisms of SLSNe are still under debate between radioactivity, circumstellar interaction (CSI), and a central engine such as magnetar spin-down (Smith & McCray 2007; Gal-Yam et al. 2009; Kasen & Bildsten 2010; Woosley 2010; Gal-Yam 2012). Since SLSNe reach an ultraviolet/optical/infrared (UVOIR) peak $\gtrsim 10^{44}$ erg s^{-1} with total radiated energy $\gtrsim 10^{51}$ erg (Gal-Yam 2012), they require $\sim$1–10 $M_\odot$ of ^{56}Ni if powered by ^{56}Ni, which is unrealistic for a core-collapse supernova (CCSN) explosion (Hamuy 2003; Smartt 2009; Curtis et al. 2019; Suwa, Tominaga & Maeda 2019). Given a CCSN explosion supplying $\sim 10^{51}$ erg of shock energy (Woosley & Janka 2005), CSI which might efficiently convert the bulk kinetic energy into radiation is one natural explanation. Some SLSNe, including Type I and Type II without narrow features, fail to exhibit evidence supporting this

★ E-mail: kbhirombhakdi@stsci.edu

Table 1. Late-time photometry of SN 2008es.

Observation date (UT)	Phase (d)	Filter	Mag (observed)	Mag (corrected)[a]	SN detection?	Telescope/ instrument	Exp. time (s)
2008-12-05	192.12	*i*	21.718 (0.068)	21.800 (0.069)	Y	P200/COSMIC	1530
2009-02-18	254.36	K'	23.494 (0.046)	23.558 (0.049)	Y	Gemini/NIRI	3120
2009-02-19	255.19	*V*	(24.449)	(24.417)	N	Keck-I/LRIS	300
2009-02-19	255.19	*g*	(25.776)	(25.737)	N	Keck-I/LRIS	420
2009-02-19	255.19	*R*	24.863 (0.298)	25.270 (0.446)	Y	Keck-I/LRIS	390
2009-02-19	255.19	*I*	23.810 (0.192)	23.928 (0.218)	Y	Keck-I/LRIS	300
2009-04-16	301.66	*H*	24.543 (0.189)	24.768 (0.234)	Y	Gemini/NIRI	3150
2009-04-16	301.66	K'	23.734 (0.118)	23.816 (0.128)	Y	Gemini/NIRI	1800
2009-06-25	359.75	*R*	(25.092)	(25.066)	N	Keck-I/LRIS	1050
2009-06-25	359.75	*I*	24.439 (0.073)	24.678 (0.095)	Y	Keck-I/LRIS	360
2009-06-27	361.41	*g*	26.436 (0.120)	(27.365)	N	Keck-I/LRIS	570
2010-01-08	523.24	*g*	(25.570)	(25.531)	N	Keck-I/LRIS	1500
2010-01-08	523.24	*R*	25.123 (0.202)	25.685 (0.352)	Y	Keck-I/LRIS	720
2010-01-08	523.24	*I*	24.765 (0.156)	25.110 (0.220)	Y	Keck-I/LRIS	480
2010-02-15	554.77	*R*	25.698 (0.142)	27.016 (0.527)	Y	Keck-II/DEIMOS	1020
2010-02-15	554.77	*I*	(25.113)	(25.095)	N	Keck-II/DEIMOS	960
2011-03-01	871.78	*g*	26.565 (0.198)	(27.304)	N	Keck-I/LRIS	1930
2011-03-01	871.78	*R*	(25.379)	(25.353)	N	Keck-I/LRIS	1180

[a]After extinction correction and host-galaxy subtraction.

explanation – strong, relatively narrow (width of a few hundred to 1000 km s^{-1}) hydrogen emission lines analogous to those of typical SNe IIn. However, recent literature (e.g. Smith & McCray 2007; Woosley, Blinnikov & Heger 2007; Chevalier & Irwin 2011; Moriya & Tominaga 2012; Smith et al. 2015; Smith 2017; Andrews & Smith 2018) discusses how narrow features could be hidden in the CSI scenario, and not observing the features cannot completely rule out the mechanism.

We have more evidence supporting that a CSI-powered hydrogen-rich supernova (SN) can show complicated evolution of the H α line. Some events might show narrow features during very early times after the explosions, and they weaken until disappearing within a few weeks, leaving only the observed broad components (Smith 2017). These objects are termed 'transitional IIn,' of which SN 1998S and PTF11iqb are examples. On the other hand, some objects show only the broad components during their light-curve peaks, and the narrow lines develop at later times. These objects constitute a 'late-time interaction' class, of which iPTF14hls (Arcavi et al. 2017; Andrews & Smith 2018) is an example. Also, we note that several of the transitional SNe IIn exhibit late-time interaction. Some late-time interacting objects that were not caught early, like iPTF14hls, might indeed show narrow features at early epochs that were missed by the time of the observations. Therefore, some objects with only broad features observed during their peaks can still be CSI SNe, which might include some SLSNe II lacking the narrow features.

Besides CSI, magnetar spin-down (Kasen & Bildsten 2010; Woosley 2010) is currently the mainstream explanation for powering SLSNe which CSI might have difficulties in explaining. Moreover, other alternatives include fall-back accretion (Dexter & Kasen 2013), or having a different explosion mechanism than CCSNe such as a pair-instability (PI) explosion (Gal-Yam et al. 2009), which can produce up to $\sim 10\ M_{\odot}$ of ^{56}Ni (Takahashi et al. 2016).

SN 2008es is one of the rare cases of an SLSN II without narrow features (Gezari et al. 2009; Miller et al. 2009). Other SLSNe II lacking narrow features include SN 2013hx and PS15br (Inserra et al. 2018). The objects in this class have only broad ($\sim$10 000 km s^{-1}) H α emission, without a narrow component. The early-time photometric data (up to $\sim$100 d) fit well to both CSI and magnetar spin-down models (Chatzopoulos et al. 2013; Inserra et al. 2018). Therefore, later-time data are required for better constraints.

Besides constraining the powering mechanism, the late-time data are informative about the circumstellar environment, which in turn constrains the progenitor's evolution. Since the SNe cool down, at late times near-infrared (NIR) emission from dust condensation is expected and has been observed in many events, especially in typical SNe II (Fox et al. 2011; Gall, Hjorth & Andersen 2011). Whether the dust emission can be similarly observed in SLSNe II, as well as whether the dust component is newly condensed from the cooling SNe or is pre-existing in the circumstellar environment, are interesting questions. SN 2006gy is one of the SLSNe II that shows an NIR excess as the sign of dust emission (Smith et al. 2008c; Miller et al. 2010; Fox et al. 2015). Here, we add SN 2008es on to the list.

In Section 2, we present late-time photometric and spectroscopic data on SLSN 2008es from 192 to 554 d after explosion in the rest frame. The data include optical and NIR bands, which give the opportunity to investigate both powering mechanism and dust. In Section 3, we show the broad H α feature with red-wing attenuation and also that there is an NIR excess, implying dust emission. Then, in Section 3, we try to explain the powering mechanism. We conclude in Section 4. Throughout, unless specified otherwise, all dates are UT, all SN phases are days after explosion in the rest frame, the assumed explosion date is MJD = 54574 and the peak of the light curve is at MJD = 54602 (Gezari et al. 2009), all magnitudes are on the AB scale (Oke & Gunn 1983), the Galactic extinction is assumed to be $E(B-V) = 0.011$ mag (Schlafly & Finkbeiner 2011), and the cosmological model is $H_0 = 70$ km s^{-1} Mpc^{-1}, $\Omega_M = 0.3$, $\Omega_\Lambda = 0.7$, $\Omega_k = 0$.

2 DATA

SN 2008es is located at $\alpha = 11^{h}56^{m}49\overset{s}{.}13$, $\delta = +54^{\circ}27'25\overset{''}{.}7$(J2000.0) at redshift $z = 0.205$ (Gezari et al. 2009). Our late-time observations include one epoch of H α spectroscopy, as shown in Fig. 2, and several epochs of optical and NIR photometry, as shown in Table 1. Aperture photometry using IRAF/DAOPHOT (Stetson 1987) was performed. Our late-time

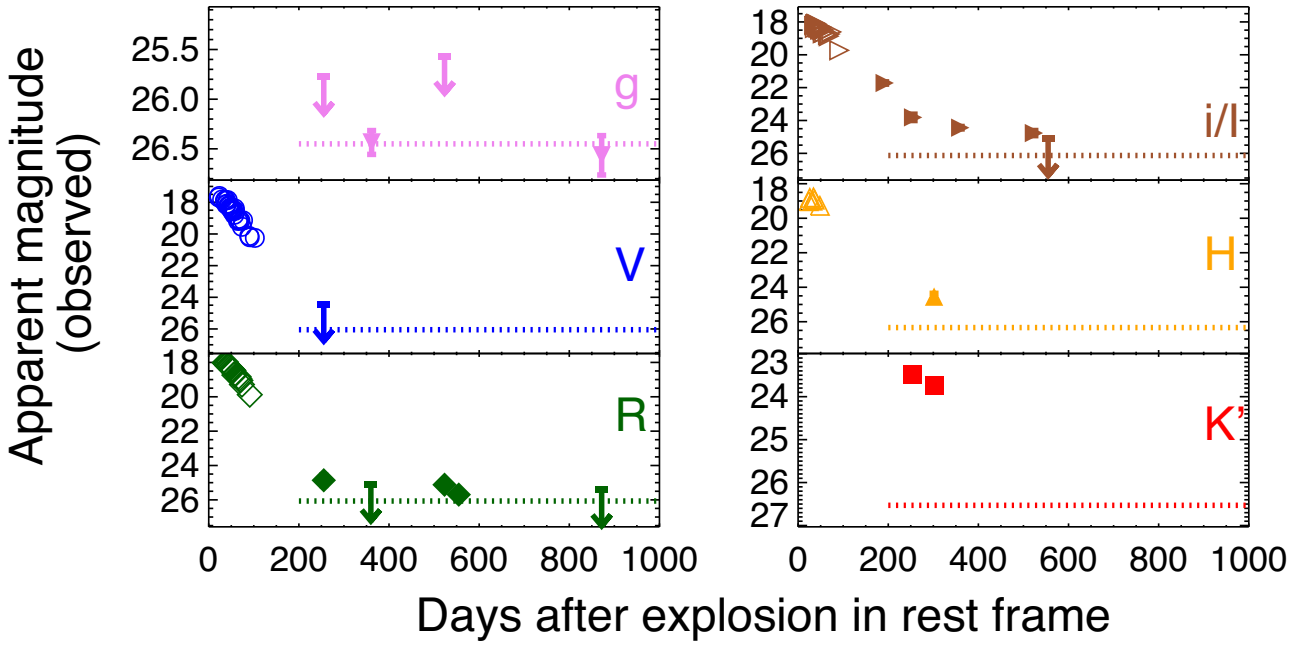

Figure 1. Photometry of SN 2008es in apparent magnitude. Filled symbols are the late-time data presented in this paper, while open symbols are the early-time data from Gezari et al. (2009) and Miller et al. (2009). Dotted horizontal line is the modelled host-galaxy emission. The figure shows that the emission in *gVR* converges to the host-galaxy light, while *IHK*′ is significantly brighter because of the strong H α emission in the *I* band and the NIR excess in the *HK*′ bands.

photometry covers 2008 December 5 (192 d) to 2010 February 15 (554 d), including one epoch from the Palomar 200-inch Hale telescope (P200) with the Carnegie Observatories Spectroscopic Multislit and Imaging Camera (COSMIC) in the *i* band,[1] several epochs of *gVRI* imaging obtained with the Low-Resolution Imaging Spectrometer (LRIS; Oke et al. 1995; Rockosi et al. 2010) on the Keck-I 10-m telescope and with the DEep Imaging Multi-Object Spectrograph (DEIMOS; Faber et al. 2003) on Keck-II, and two epochs of *HK*′ from the Near InfraRed Imager and spectrograph (NIRI) on Gemini (Hodapp et al. 2003). Additionally, we acquired *gR* photometry from the public Keck Observatory Archive (KOA), extending the coverage to 2011 March 1 (871 d).

We obtained a single 2000 s spectroscopic exposure using the Gemini Multi-Object Spectrograph (GMOS; Hook et al. 2004) on the 8-m Gemini-North telescope on 2009 March 31.5 (288 d). Our instrumental set-up used the R400 grating and a 1.0-arcsec-wide slit to cover the observed spectral range of 5500–9750 Å at a resolution of 7 Å. We used standard IRAF[2] tasks to perform two-dimensional image processing and spectral extraction, as well as custom IDL routines to apply a relative flux calibration using an archival standard star. At the position of the transient, a very faint trace is barely detected in the continuum. However, a single broad emission feature is present at 7650–7950 Å, which we identify as H α emission from the SN.

For photometric data, images of SN 2008es were reduced by following the usual procedures (bias, dark, flat, and photometric calibration) in IRAF. The data on 2011 March 1 were stacked from two different epochs to increase the signal-to-noise ratio (S/N): 2011 February 1 and 2011 March 26. Up to nine standard stars were identified in the field of images from the Sloan Digital Sky Survey (SDSS) Eighth Data Eelease (DR8) catalogue for optical bands (*ugriz*), which were transformed to *UBVRI* by following Blanton & Roweis (2007). We calibrated the LRIS *g*-band images to SDSS *g* (the two bands differ slightly). For NIR bands, the star FS 21 observed on 2009 April 16 was taken as the standard for calibrating *HK*′ at the same epoch, while *K*′ on 2009 February 18 was calibrated by creating a catalogue from the stars in the field observed on 2009 April 16. The quality of the created catalogue was verified with a few stars present in the field of view and tabulated in the 2-Micron All-Sky Survey catalogue. We converted magnitudes from Vega system to AB by following Blanton & Roweis (2007), Breeveld et al. (2011), and Tokunaga & Vacca (2005). For consistency with the other observations of SN 2008es, we transformed the *i*-band data from 2008 December 5 to the *I* band using $I(\mathrm{AB}) = i(\mathrm{AB}) - 0.518$, found by assuming constant colour from 2009 February 19 with the transformation equations from Blanton & Roweis (2007). This was a reasonable assumption, since SN 2008es converged to a temperature of $T = 5000$–6000 K by the end of the early-time observations (Gezari et al. 2009; Miller et al. 2009).

Table 1 shows the observed AB magnitudes for the source at the position of the SN, both before and after correction for host-galaxy contamination and the Galactic extinction. Some data are marked as non-detections because their fluxes are less than 3σ above zero; these data are reported as 3σ upper limits (in parentheses). Fig. 1 plots the late-time data, including the earlier time data from Gezari et al. (2009) and Miller et al. (2009).

A faint ($M_R \approx 26$ mag) host galaxy of SN 2008es has been previously reported (Angus et al. 2016). The late-time data tend to converge to constants, corresponding to the host emission. Host subtraction was performed numerically owing to the lack of template images in several filters and the low significance of

[1] http://www.astro.caltech.edu/palomar/observer/200inchResources/cosmicspecs.html

[2] IRAF is distributed by the National Optical Astronomy Observatory, which is operated by the Association of Universities for Research in Astronomy (AURA), Inc., under cooperative agreement with the National Science Foundation (NSF).

Table 2. Host emission of SN 2008es (no extinction correction).

Filter	Mag (measured)[a]	Mag (modelled)[b]
B	26.96 (0.25)	26.75 (0.08)
g	26.44 (0.27)	26.45 (0.08)
V	–	26.05 (0.08)
R	25.96 (0.20)	26.07 (0.08)
I	–	26.13 (0.08)
*F*160*W*/*H*	26.85 (0.40)	26.34 (0.08)
$K^{'}$	–	26.53 (0.08)

[a]From Angus et al. (2016) and Schulze et al. (2018).
[b]Uncertainties come only from the estimate of the normalization constant.

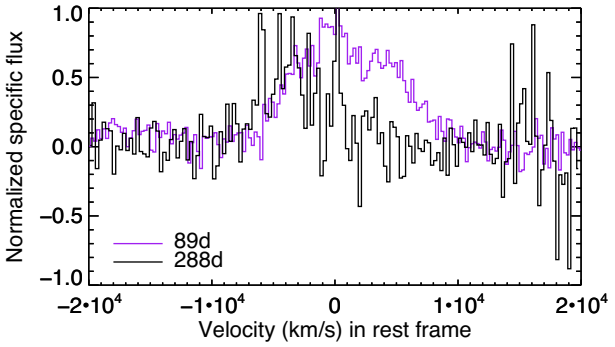

Figure 2. SN 2008es spectra, centred at H α, at 89 (purple; Miller et al. 2009) and 288 (black) days after explosion in the rest frame. A linear continuum has been subtracted from each spectrum to isolate the line emission. Both spectra are normalized to unity at peak for comparison purposes. We note that the narrow spikes in the late-time spectrum are noise caused by sky-subtraction residuals. The late-time spectrum shows red-wing attenuation, and stronger EW of H α emission compared to the earlier one.

several of the detections, including those of the host only. A Galactic extinction correction was applied. Host-galaxy extinction was assumed to be negligible because the host of SN 2008es is blue and has low metallicity (Angus et al. 2016; Schulze et al. 2018). Host subtraction was performed by adopting a host-galaxy model from Starburst99 (Leitherer et al. 1999, 2010; Vázquez & Leitherer 2005; Leitherer et al. 2014). These templates are simulated for an instantaneous burst of star formation, given an initial mass function with power-law index 2.35 over the range of 1–100 $M_{\odot}$, and nebular emission is included. The templates include metallicity 0.001–0.04 and age 1–900 Myr.

The best galaxy model was selected by fitting the measured *BgR*/*F*160*W* emission of the host of SN 2008es from Angus et al. (2016) and Schulze et al. (2018), as shown in Table 2. We note that the host images in the bands *BR* and *F*160*W*, which is equivalent to the *H* band, were taken at phase ∼1700 d, much later than the last *H* data presented in Fig. 1. We assume that there is no SN contamination at ∼1700 d. The best-fitting galaxy, determined by the lowest summed squared residuals, has metallicity 0.001 and an age of 200 Myr, consistent with the results of Schulze et al. (2018). The host emission was then estimated from the best-fitting galaxy model for each band, as shown in Table 2; Fig. 1 also shows the modelled host emission. We note that the estimated uncertainties of the modelled emission are unrealistically low, because only the statistical error from estimating the normalization factor is included. However, as we will see, our analysis is insensitive to this.

We apply the modelled host emission to perform the host subtraction. Table 1 shows corrected AB magnitudes of the late-time data after extinction correction and host subtraction. We also note that in this column the *i*-band data are also transformed into the *I* band. Some data, which are detections before the correction, are marked as non-detections because the corrected fluxes are less than 1σ above zero; therefore, these data are reported as 3σ upper limits (in parentheses). For some data that are marked as non-detection before the subtraction, only the extinction correction is applied, and the data are reported as 3σ upper limits. For a quick summary, Table 1 provides a column noting whether the data after the correction are considered to be SN detections.

3 ANALYSIS AND DISCUSSION

In this section, we analyse the data of SN 2008es and discuss the implications. First, we look at the H α emission, which exhibits a sign of dust condensation in the cool dense shell (CDS) and strong CSI but still shows no sign of narrow absorption/emission features. Then, we demonstrate that there exists an NIR excess corresponding to the thermal dust emission in the CDS. Last, we verify that CSI is the preferred powering mechanism, which is still the dominant mechanism during the late-time epochs.

3.1 Spectroscopy: strong CSI and CDS dust condensation

It is common in SNe II that strong CSI leads to the formation of a CDS, and dust condensation in this region at early times (i.e. $\lesssim$500 days), earlier than the expectation of dust forming in the inner ejecta (Pozzo et al. 2004; Smith, Foley & Filippenko 2008a; Smith et al. 2008b, 2009b, 2012; Andrews et al. 2010, 2016; Fox et al. 2011; Gall et al. 2011; Stritzinger et al. 2012; Gall et al. 2014). The CDS is the region in between the forward and reverse shocks. A thermal instability can develop in this region, resulting in efficient cooling and increased density (Chevalier & Fransson 2017). Additionally, the cooling is enhanced by metals in the ejecta. Because of this, dust condensation is very likely, and has been observed in many events (Andrews et al. 2010, 2016; Fox et al. 2011).

To confirm dust condensation in the CDS, multiple pieces of evidence should be observed consistently. These include strong CSI, infrared excess, red-wing attenuation of spectral features, and the early onset (i.e. $\lesssim$500 d) of these observational features (Andrews et al. 2010, 2016; Fox et al. 2011; Gall et al. 2011).

3.1.1 H α emission and strong CSI

From the light curves presented in Fig. 1, we note the persistent excess flux in the *I* band. Fig. 3 shows the excess relative to the assumed continuum of a 5000 K blackbody scaled to the *R* band. We assume a continuum blackbody temperature of 5000 K because there is evidence from the early-time analysis (Gezari et al. 2009; Miller et al. 2009) that the temperature was converging to this value, which corresponds to the temperature of hydrogen recombination.

The excess *I*-band flux comes from strong-line emission, as shown in Fig. 2, which presents spectra from the bandpass equivalent to the *I* band. We clearly see the strong H α line emission.

The prominent H α emission implies strong CSI. We can quantitatively show this by estimating the luminosity of H α emission and its equivalent width (EW). We cannot estimate the luminosity of H α directly from the spectra owing to the lack of an absolute calibration, so we instead apply a photometric scaling from

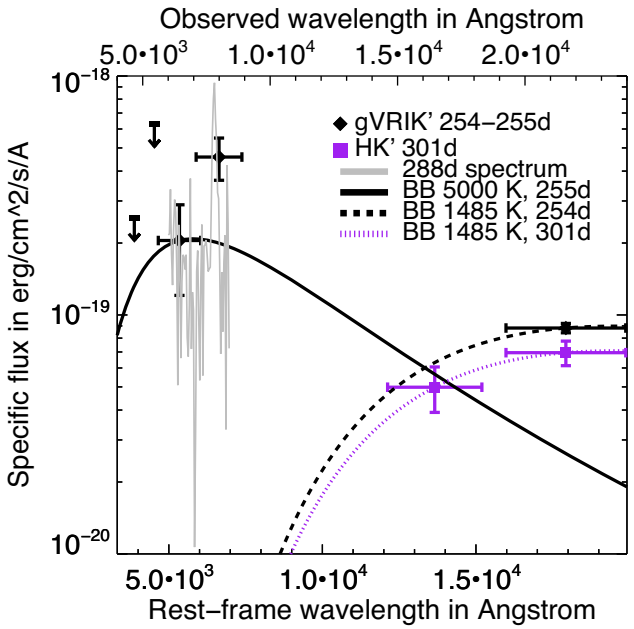

Figure 3. NIR excess. Data points are $gVRIK'$ (black, diamond) at 254–255 d, and HK' (purple, square) at 301 d. Solid grey line is the 288-d spectrum scaled to the R band, showing H α contamination in the I band. Solid black line is the 5000 K blackbody optical component, fit to the R data at 255 d. Dashed black line is the 1485 K blackbody NIR component, scaled to the K' data at 254 d. Dotted purple line is the 1485 K blackbody NIR component, fit to the HK' data at 301 d. Downward black arrow is the 3σ upper limit of the gV bands at 255 d.

observations at 255 d. The I-band data have contributions from both the H α emission and the continuum, so we subtract the assumed continuum of a 5000-K blackbody scaled to the R band, as shown in Fig. 3. The estimate yields $\sim 5 \times 10^{40}$ erg s^{-1} of H α emission at 255 d; at a similar epoch, this is comparable to some well-studied SNe IIn (e.g. SN 1988Z, Turatto et al. 1993; SN 1998S, Mauerhan & Smith 2012) and to SLSNe-II with narrow features (e.g. SN 2006gy, Smith et al. 2010).

We can measure the EW of the H α emission directly from the spectra: 807 Å at 288 d and 161 Å at 89 d. We note that, relative to the continuum estimated from the vicinity around the emission, H α emission at 255 d is significantly stronger than that of 89 d. At similar epochs, the 288-d EW is comparable to those of SN 1988Z (Type IIn; Stathakis & Sadler 1991; Turatto et al. 1993) and SLSN 2006tf (a SLSN II with narrow features; Smith et al. 2008b), and significantly stronger than that of SLSN 2006gy (Smith et al. 2010). The increasing trend of the EW of H α emission with time is also common in SNe IIn, which are powered by CSI, although the SLSN 2006gy does not exhibit such a trend (Smith et al. 2008b, 2009b, 2010).

3.1.2 Blueshifted H α and CDS dust condensation

Red-wing attenuation of spectral features is expected, but not always, if dust is formed in the CDS (Andrews et al. 2010, 2016; Fox et al. 2011; Gall et al. 2011). Observationally, the red-wing attenuated spectra show blueshifted peaks, and asymmetry by having the red-side emission weaker than that of the blue side, because dust in the CDS obscures more of the emission from the far side than from the near side. Progressively stronger attenuation with time is also expected as increasing amounts of dust are formed.

Fig. 2 compares the shape of the 89-d and 288-d spectra of H α emission. The blueshifted peak in the 288-d spectrum is evident, while the maximal velocity of the blue-wing at $\sim$10 000 km s^{-1} is similar to that of the 89-d one. This evidence, together with strong CSI and the early onset (i.e. at least before 288 d), supports the interpretation of dust condensation in the CDS.

Last, we note two other possible scenarios causing the observed blueshifted peak. First is the asymmetry of the ejecta, with a higher concentration of radioactive material (i.e. ^{56}Co during these epochs) towards the near side along the line of sight yielding more excitation and, therefore, more emission from the blue-wing (Hanuschik, Thimm & Dachs 1988; Elmhamdi et al. 2003; Gall et al. 2011). However, this is unlikely because ^{56}Co is not significantly powering the light curve (see Section 3.3). Second is asymmetry of the CSM, with a higher concentration of CSM towards the near side of the ejecta enhancing the blue-wing emission (Smith 2006; Andrews et al. 2017). This scenario cannot be ruled out but is less favoured, compared to the interpretation of CDS dust, because it does not explain the observed NIR excess. We show evidence of an NIR excess and discuss its implications in the next section.

3.2 NIR Excess: CDS Dust Emission

Here, we will present the evidence for an NIR excess consistent with the interpretation of CDS dust condensation. The $gVRIK'$ photometry at 254–255 d and HK' photometry at 301 d are shown in Fig. 3. We note that the observations in the gV bands are non-detections and the 301-d HK' data are not contemporaneous with the optical $gVRIK'$ data – about 50 d difference. To show the NIR excess, we fit the $gVRIK'$ data at 254–255 d with two blackbody components, optical and NIR. The optical $gVRI$ component is assumed to have $T = 5000$ K, as implied by the photospheric temperature evolution shown in the early-time analysis (Gezari et al. 2009; Miller et al. 2009), and scaled to the R band (because gV are non-detections and I is contaminated by H α emission). For the NIR K' component, since we cannot fit the blackbody function or the temperature to a single data point, we estimate the flux by fitting the temperature from the HK' data at 301 d, and assuming a constant value over the range of 254–301 d. We note that the contribution of the optical component at 301 d to the NIR component at the same epoch appears to be insignificant. We estimate this by scaling the same 5000 K blackbody component to the interpolated R flux at 301 d.

As shown in Fig. 3, the NIR excess relative to the optical photosphere is evident. This NIR component has a blackbody temperature of 1485 K. The NIR excess about a year after the explosion supports the existence of thermal dust emission (Fox et al. 2011; Gall et al. 2011).

Next, we provide supporting evidence that the dust emitting this NIR excess is the CDS dust by showing that, first, the photospheric radius of the NIR component is located around the CDS region, and secondly, the radius is inconsistent with alternative explanations associated with CSM dust.

With the 1485 K temperature, we estimate the bolometric luminosity of the NIR component, shown in Table 3, by simply integrating the blackbody function. The implied photospheric radius is $\sim 10^{16}$ cm. The radius corresponds to the location of the forward shock, assuming an expansion velocity of 10 000 km s^{-1} as implied by the spectra. The correspondence of the location of

Table 3. Bolometric luminosity of the NIR component.

Phase (d)	$\log_{10}[L]$ (erg s^{-1})	Temperature (K)	Radius (cm)
254.36	41.59 (0.45)	1485[a]	1.06×10^{16}
301.66	41.49 (0.45)	1485 (218)	9.41×10^{15}

[a]Assumed 1485 K from 301 d.

the forward shock and the NIR component strongly supports the hypothesis that the CDS dust is responsible for emitting the observed thermal NIR excess; this is similar to the NIR-emitting CDS dust observed in some events such as SN 2005ip (Type IIn; Fox et al. 2009; Graham et al. 1983). Moreover, the ∼1500 K temperature of the NIR component is reasonable for the dust-condensation temperature.

The observed NIR excess is inconsistent with other explanations involving CSM dust emission (e.g. collision of ejecta, Graham et al. 1986; IR echo, Dwek 1983) because the blackbody radius of $\sim 10^{16}$ cm is significantly smaller than the size of the dust-free cavity, at $\sim 10^{17}$ cm, for typical parameters of SLSNe. The size of the dust-free cavity $R_{\rm evap}$ created by the SN peak flash is estimated from (Dwek 1983)

$$R_{\rm evap} = (23\,{\rm pc}) \left(\frac{\bar{Q}_{\rm evap}\,(L_{\rm peak}/{\rm L}_\odot)}{(\lambda_{\rm d}/\mu{\rm m})\,T_{\rm evap}^5} \right)^{0.5}, \quad (1)$$

where $\bar{Q}_{\rm evap}$ is the mean grain emissivity, $L_{\rm peak}$ is the peak luminosity, $\lambda_{\rm d} = 2\pi a$ (a is the radius of dust grain), and $T_{\rm evap}$ is the dust-evaporation temperature in kelvins. By assuming typical parameters for graphite grains of $\bar{Q}_{\rm evap} = 1$, $a = 0.1$ μm, and $T_{\rm evap} = 1900$ K, the peak flash of SN 2008es creates a dust-free cavity of size $\sim 10^{17}$ cm. We also note that this value tends to be a lower limit, since the size is sensitive to the evaporation temperature that is significantly lower for other dust species, such as 1200 K for silicate grains (Dwek 1983, 1985; Fox et al. 2009, 2010).

Our analysis is sensitive to only the warm dust that emits at NIR wavelengths. Colder dust, which lies farther away (e.g. in the CSM), might exist and emit at longer wavelengths via mechanisms such as an IR echo, which is observed in SLSN 2006gy at epochs similar to those of our late-time observations (Miller et al. 2010; Fox et al. 2015). However, the emission from cold dust, if it exists, does not affect our interpretation of the warm dust. Also, we note that the spectral energy distribution is assumed to be a blackbody in our analysis.

3.3 Powering Mechanisms

In this section, we discuss possible powering mechanisms of SN 2008es, specifically CSI and magnetar spin-down (Gezari et al. 2009; Miller et al. 2009; Chatzopoulos et al. 2013; Inserra et al. 2018). Both candidates fit well with the early-time data, and can be constrained better by our later-time data. We start by discussing the evolution of the light curve in general. Then, we show that CSI is preferred and yields implications consistent with other observed evidence. However, we also show that magnetar spin-down cannot be ruled out (but is less favoured).

3.3.1 Evolution of the light curve of SN 2008es

The evolution of the light curve of SN 2008es is shown in Fig. 1 for each filter (as discussed in the previous section), and in Fig. 4 for the bolometric luminosity, including the early-time data from

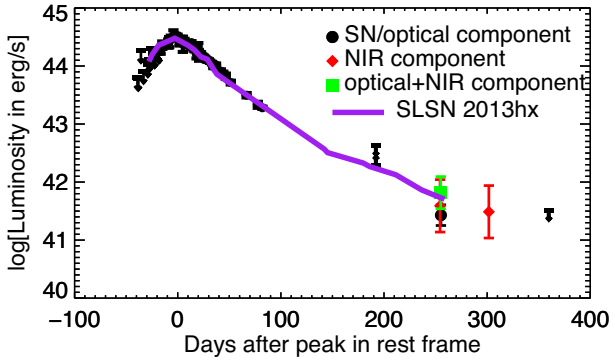

Figure 4. Bolometric luminosity of SN 2008es compared with SN 2013hx. Circle (black) is the optical component, diamond (red) is the NIR component, square (green) is the optical+NIR component, downward arrow is the 3σ upper limit, upward arrow is the 3σ lower limit, solid line (purple) is the bolometric luminosity of SN 2013hx (Inserra et al. 2018).

Table 4. Bolometric luminosity of late-time optical component.

Phase (d)	$\log_{10}[L]$ (erg s^{-1})	Temperature[a] (K)	Radius (10^{14} cm)
192.12	42.28–42.63[b]	5000	20.7–31.0
255.19	41.43 (0.18)	5000	7.76
359.75	<41.51	5000	<8.52

[a]Assumed to be 5000 K.
[b]See the text for the estimation of lower and upper limits.

Gezari et al. (2009) and Miller et al. (2009) as well as our later-time data from Tables 3 and 4. When determining the bolometric luminosity, we estimate separately the NIR excess component from the SN component, so that we can investigate the contribution from each component. The bolometric luminosity of the SN component, which we refer to as the optical component, is estimated by simply integrating the 5000 K blackbody. At day 192, our only observation is in the i band, which is potentially contaminated by H α emission. We set an upper limit by scaling the blackbody to the I band, which is equivalent to assuming negligible H α contamination. The lower limit is estimated by assuming constant $R - I$ colour from 255 d. This sets a lower limit since the colour at 192 d can be bluer than assumed if the EW of H α emission is increasing with time. At 359 d, the upper limit is estimated from the 3σ upper limit in the R band. For the rising part, the data from ROTSE-IIIb of Gezari et al. (2009) are transformed into equivalent R-band points by using the data near peak. Then we assume a constant temperature during the rise to the peak to estimate the bolometric luminosity. For the NIR excess component, we integrate the 1485 K blackbody function for the bolometric luminosity.

The bolometric light curve has a peak of $\sim 3 \times 10^{44}$ erg s^{-1}, and the estimated explosion is at about 23 d (Gezari et al. 2009). (Note that Fig. 4 shows days after peak brightness.) Then it linearly decays (in magnitude) until the end of the early-time data. At later times, the NIR component shows a slow decay rate of 0.005 ± 0.003 mag d^{-1}estimated from the two K' epochs. If ^{56}Co were powering the NIR component, this would set an upper limit to the initial ^{56}Ni mass of $\lesssim$0.4 M$_\odot$ by scaling the luminosity from ^{56}Co decay to the NIR components. We note that the evolution of the optical component depends on whether the constraints from a single band (i) at 192 d are correct.

In addition, Fig. 4 shows the bolometric light curve of SN 2013hx (Inserra et al. 2018), which is also a SN II lacking narrow features. Although the light curves are strikingly similar, the spectral evolution of the two objects differs, leading to different interpretations. While our spectra of SN 2008es show red-wing attenuation, implying the existence of dust formation, the spectra of SN 2013hx exhibit H α emission with multiple peaks and multiple velocity components, implying interaction with asymmetric CSM (Inserra et al. 2018). At ∼300 d after peak brightness, SN 2013hx shows brighter emission in the K band relative to optical bands (Inserra et al. 2018), hinting at a possible NIR excess. However, there is not enough information to verify this, and whether dust emission exists in SN 2013hx is an interesting question deserving of future investigation. Besides SN 2013hx, another SLSN II lacking narrow features is PS15br (Inserra et al. 2018), whose light curve evolves differently, with a slower decay rate after peak compared to SN 2008es and SN 2013hx.

3.3.2 CSI

Efficient conversion of shock energy to radiation by CSI seems to be a natural explanation for the powering mechanism in SLSNe II with narrow features, such as SLSN 2006gy (Ofek et al. 2007; Smith et al. 2007). Although SLSN 2008es lacks narrow features, the CSI model fits its bolometric light curve well at early times. Here, we include our later-time data in a similar analysis for a better constraint on the mechanism.

We apply a semi-analytical model of CSI by using the CSMRAD routine in the TigerFit package.[3] Similar to Chatzopoulos, Wheeler & Vinko (2012), Chatzopoulos et al. (2013), and Wheeler et al. (2017), this model implements CSI with a diffusion process, including forward/reverse shock interaction, and radioactive (i.e. ^{56}Ni and ^{56}Co) heating. Parameters in the model include the initial ^{56}Ni mass $M_{\rm Ni}$, explosion energy $E_{\rm SN}$, progenitor radius $R_{\rm p}$ (which is equivalent to the inner radius of the CSM in this model), ejecta mass $M_{\rm ej}$, ejecta opacity $\kappa_{\rm ej}$, power-law index of the density profile of the inner ejecta d and of the outer ejecta n, power-law index of the density profile of the CSM s, CSM mass $M_{\rm CSM}$, mass-loss rate $\dot{M}$, and CSM wind velocity $v_{\rm w}$. We note that, because of the large parameter set and non-linearity of the model, the model tends to have high degeneracy that yields non-unique solutions with some uncertainty. Therefore, determining the best fit requires careful inspection.

Table 5 shows four selected best-fitting results. CSMRAD1 and CSMRAD3 are fed with only the early-time data, while the others also have the 192-d and 255-d (only optical component) data in the fit. We include the 192-d data by using the average and dispersion of the lower and upper limits. CSMRAD1 and CSMRAD2 assume a uniform density distribution ($s = 0$), while the others assume a steady wind ($s = 2$). To be comparable with the results of Chatzopoulos et al. (2013) and Inserra et al. (2018), all models assume a power-law index of 2 ($d = 2$) for the density profile of the inner ejecta. We note that the solutions are insignificantly changed when applying $d = 0$, which is another common value used in the literature (Wheeler et al. 2017). Also, we note that in the table, we present the outer radius of the CSM $R_{\rm CSM}$ and the CSM density $\rho_{\rm CSM}$ instead of the mass-loss rate and the wind velocity by applying $\rho_{\rm CSM} = \dot{M}/(4\pi v_{\rm w} R_{\rm p}^2)$ and $R_{\rm CSM} = [3M_{\rm CSM}/(4\pi\rho_{\rm CSM} R_{\rm p}^s) + R_{\rm p}^{3-s}]^{1/3}$ (see Chatzopoulos et al. 2012 and also the code in TigerFit). Fig. 5 shows these models, demonstrating that they are degenerate at early times but are distinguishable at later times. According to our coverage, we still cannot determine with certainty the best model among the four. It is interesting to note that, with only the early-time data, the solutions (CSMRAD1 and CSMRAD3) also fit well the later-time data, supporting the continuation of CSI as the dominant power source from early to late times.

The results of uniform-density models fit with only the early-time data (CSMRAD1) are comparable to previous estimates in the literature (Miller et al. 2009; Chatzopoulos et al. 2013; Inserra et al. 2018). For all models, the results show similar properties for the progenitor and CSM. The estimate indicates a low mass of ^{56}Ni, implying that it is not the dominant source of energy during our observational epochs. The explosion energy is ∼5 × 10^{51} erg with

[3] https://github.com/manolis07gr/TigerFit

Table 5. Fit results from CSMRAD model from TigerFit.

Parameters	CSMRAD1	CSMRAD2	CSMRAD3	CSMRAD4
data[a]	early	early+late	early	early+late
s	0	0	2	2
$M_{\rm Ni}$ ($M_\odot$)	0.012	0.001	0.000	0.039
$E_{\rm SN}$ (10^{51} erg)	5.856	5.800	5.155	5.427
R_p (10^{14} cm)	5.072	4.617	1.761	1.707
$M_{\rm ej}$ ($M_\odot$)	11.591	11.271	16.308	15.473
$\kappa_{\rm ej}$ (cm^{2}g^{-1})	0.30	0.30	0.36	0.34
d	2	2	2	2
n	12	11	12	12
$M_{\rm CSM}$ ($M_\odot$)	2.668	2.349	2.647	2.491
$R_{\rm CSM}$ (10^{14} cm)	12.759	11.672	15.574	13.417
$\rho_{\rm CSM}$ (10^{-13} g cm^{-3})	6.544	7.519	98.249	116.138
Reduced χ^2	3.643	3.267	3.669	4.851

[a] Fit with early-time data, or including late-time data at 192 and 255 d.

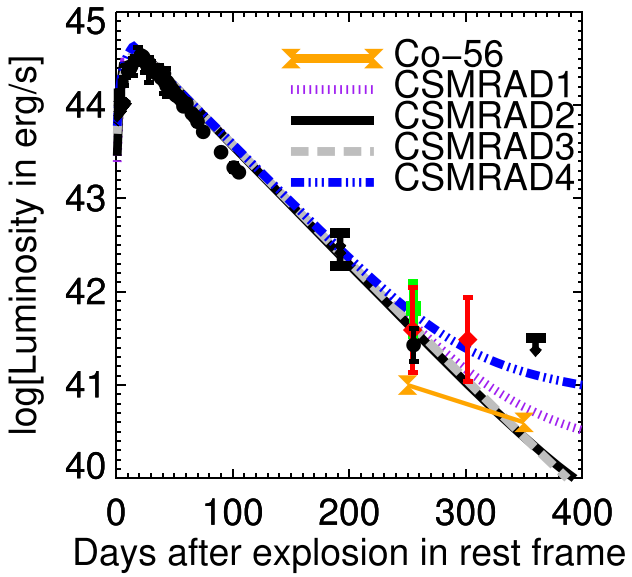

Figure 5. Bolometric luminosity of SN 2008es with models of CSI and ^{56}Ni powering. Circle (black) is the optical component, diamond (red) is the NIR component, square (green) is the optical+NIR component, solid line with hourglass (orange) is ^{56}Co decay, dotted line (purple) is CSMRAD1, solid line (black) is CSMRAD2, dashed line (grey) is CSMRAD3, dot-dot-dot-dash line (blue) is CSMRAD4.

ejecta mass ∼10–20 $M_\odot$. The effective CSM mass is ∼2–3 $M_\odot$, which is comparable to that of SN 2006tf (superluminous SN II with narrow features; Smith et al. 2008b), but less than that of SN 2006gy with ∼10 $M_\odot$ (Miller et al. 2010). Comparing to typical SNe IIn, which have CSM mass ∼0.1–10 $M_\odot$ (Branch & Wheeler 2017), the estimated CSM mass of SN 2008es is greater than that of SN 2005ip, which had ∼0.1 $M_\odot$ (Smith et al. 2009b), and comparable to that of SN 2010jl (Andrews et al. 2011), but less than that of SN 1988Z (∼10 $M_\odot$; Aretxaga et al. 1999). The effective outer radius of the CSM is $\sim10^{15}$ cm, comparable to the photospheric radius at peak brightness and supporting the CSI mechanism. For the steady-wind models, the mass-loss rate is ∼0.1–1 $M_\odot\,yr^{-1}$, given a wind velocity of ∼100 $km\,s^{-1}$, and for the uniform-density models, the CSM density is $\sim10^{-12}$–10^{-13} $g\,cm^{-3}$.

We investigate the potential radio-emission properties of this CSI given the large derived mass-loss rate of 0.1–1 $M_\odot\,yr^{-1}$ and the explosion energy $\sim5\times10^{51}$ erg estimated in the steady-wind models following Chevalier (1998), Chevalier & Fransson (2006), and Soderberg et al. (2012), as synthesized by Coppejans et al. (2018) and assuming similar microphysical parameters. The synchrotron radio emission is heavily self-absorbed at all early times when the shock is located within R_{CSM} derived above, but if the wind extends to a large radius we estimate the 5 GHz synchrotron radio emission to reach its peak at ∼1 mJy (i.e. $\sim10^{30}$ erg s^{-1} Hz^{-1}) at an age of 6–20 yr, corresponding to an interaction region at a radius of $\sim10^{17}$ cm from the explosion site. However, it is unphysical for a steady wind with such a high mass-loss rate to extend to this large radius without truncation because the total mass in the wind would be very large, and so the true peak radio flux will lie below this estimate. Therefore, any prediction is uncertain because it depends on the CSM density at larger radii than those probed by the optical light curve presented in this work.

We note that the estimated mass-loss rate of SN 2008es is very high compared to known massive stellar winds, at most $\lesssim10^{-3}$ $M_\odot\,yr^{-1}$ with $v_w\approx10$ $km\,s^{-1}$ for extreme red supergiants (RSGs; Smith 2014; Vink 2015; Smith 2017). The mechanism for this extreme mass-loss a few years before the explosion is still unknown, but is believed to be either by binary interaction ($\lesssim10^{-1}$ $M_\odot\,yr^{-1}$ with $v_w\approx$ 10–100 $km\,s^{-1}$) or a luminous blue variable (LBV)-like giant eruption ($\lesssim10$ $M_\odot\,yr^{-1}$ with $v_w\approx$ 100–1000 $km\,s^{-1}$) such as those observed in η Carinae or P Cygni (Smith et al. 2003; Smith & Hartigan 2006; Smith & Owocki 2006; Chevalier 2012; Smith 2014, 2017). The inferred mass-loss rates for most strong CSI events (such as SLSNe 2006gy and 2006tf, and SN IIn 2010jl) are consistent with those of giant eruptions, while the mass-loss rates of some SNe IIn (such as SNe 1988Z and 1998S) are consistent with those of binary interaction (Smith 2017). For SN 2008es, the estimated mass-loss rate is consistent with that of a giant eruption. Other proposed extreme mass-loss mechanisms include hydrodynamic instabilities (Smith & Arnett 2014), gravity-wave-driven mass-loss (Shiode & Quataert 2014), or centrifugal-driven mass-loss of spun-up Wolf–Rayet stars (Aguilera-Dena et al. 2018), which might be more related to the hydrogen-poor events rather than to the hydrogen-rich ones.

Regardless of what exact mechanism caused the extreme mass-loss, the CSM structure is unlikely to have a steady-wind profile, but is more likely approximated by a dense shell of uniform density (Chatzopoulos et al. 2012). Therefore, the CSI with wind models (i.e. CSMRAD3 and CSMRAD4) are less favoured compared to the uniform-density ones. Also, the estimates assume spherical symmetry, yet it is likely that the CSM structure is actually complex. With bipolar/disc/torus shapes, multiple shells, or clumpy structure (Smith 2006; Smith, Hinkle & Ryde 2009a; Andrews et al. 2010, 2016; Smith 2014), the mass-loss rate can be lower than that derived for spherical symmetry.

Our fit results strongly support CSI as the powering mechanism of SN 2008es. Moreover, the interpretation of CSI powering both the early-time and later-time emission is consistent with the high EW of H α and the existence of CDS dust, as discussed in the previous section.

Finally, we note that because it lacked narrow features, SN 2008es was argued to be inconsistent with the CSI powering scenario (Gezari et al. 2009). However, recent literature (Smith & McCray 2007; Woosley et al. 2007; Chevalier & Irwin 2011; Moriya & Tominaga 2012; Smith et al. 2015; Andrews & Smith 2018) discusses how this is feasible with some CSM configurations, for example, if the CSM is shocked and accelerated to high velocities before the shock breaks out. Therefore, a luminous SN without narrow features can be powered by strong CSI. Similar objects of this nature are also known for being transitional SNe IIn or late-time interacting SNe II (Smith 2017). These objects include (for example) iPTF14hls, which was an interacting hydrogen-rich SN hiding its narrow features until about 3 yr after discovery (Arcavi et al. 2017; Andrews & Smith 2018), and PTF11iqb, which was discovered when it had a narrow H α emission line that weakened quickly thereafter (Smith et al. 2015). Without performing coupled hydrodynamic and radiative transfer simulations, we cannot definitively determine whether SN 2008es is consistent with being powered by one of these scenarios. However, we support our claim by following the analytic estimates presented by Chevalier & Irwin (2011) for the steady-wind case and Moriya & Tominaga (2012) for the uniform-density case.

Chevalier & Irwin (2011) considered the case of a steady-wind CSM and formulated the conditions determining whether shock breakout occurred inside or outside the optically thick CSM. For the case of a shock breaking outside, the CSM is shocked and accelerated before breakout, leaving only minimal unshocked CSM so that the SN exhibits no narrow spectral features. This happens when the outer CSM radius R_w is smaller than the diffusive radius (or breakout radius) R_d. In this case, the time-scale since when photons can emerge from the optically thick CSM to its peak (i.e. the rising time t_r) is $R_w^2/(vR_d)$, where v is the shock velocity. This directly implies $t_r < R_d/v \approx 6kD_*$ day, where $k=\kappa/0.34$ $cm^2\,g^{-1}$, κ is the opacity, and $D_* = [\dot{M}/(10^{-2}M_\odot\,yr^{-1})]/[v_w/(10\,km\,s^{-1})]$ is the density parameter. From the best-fitting TigerFit models with a steady wind, $D_*\approx8$. With $k=1$ for the typical opacity in hydrogen-rich SNe and the observed rise time-scale of 23 d for SN 2008es, the condition is satisfied.

Moriya & Tominaga (2012) considered the complementary situation of a uniform density configuration and found some cases where SLSNe II powered by CSI lacked narrow features (their fig. 1). In this scenario, the condition $vt_{LC}/R_w \geq 1$, where t_{LC} is the effective light-curve time-scale, is necessary. Given a typical characteristic shock velocity and $R_w \gtrsim 10^{15}$ cm, the rise time-scale of 23 d, which is typically assumed to be a proxy for the light-curve time-scale, satisfies the condition.

Last, we note that further thorough investigations of how a strongly interacting SN can hide the narrow features are necessary. Since asymmetry might play important roles in this scenario, two-dimensional or three-dimensional hydrodynamic simulations are required.

Table 6. Fit results from magnetar model[a].

Parameters	MAG1	MAG2
Trap[b]	O	I
t_{LC} (d)	19.47 (4.66)	18.94 (2.40)
t_p (d)	23.88 (19.96)	23.92 (8.67)
E_p (10^{51} erg)	2.41 (1.42)	2.34 (0.58)
A (d^2)	5424 (4576)	5173 (1854)
P (ms)	2.88	2.92
B (10^{14} G)	1.28	1.30
M_{ej} ($M_\odot$)	0.53	0.50
$L(t = 255)$ (erg s^{-1})	1.2×10^{42}	1.2×10^{42}
$L(t = 302)$ (erg s^{-1})	7.1×10^{41}	6.9×10^{41}
$L(t = 360)$ (erg s^{-1})	4.0×10^{41}	3.9×10^{41}
Reduced χ^2	5.54	4.48

[a]Uncertainties in parentheses.
[b]Implementation of trapping function (O = outside integral, I = inside).

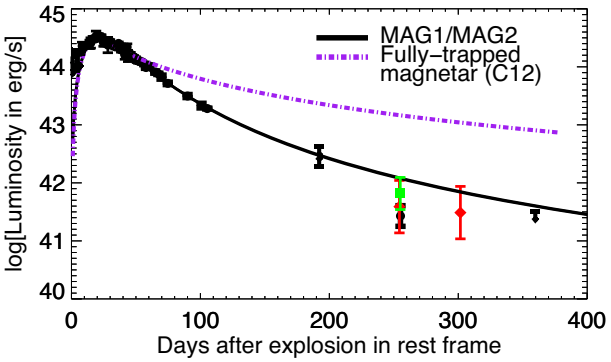

Figure 6. Bolometric luminosity of SN 2008es with magnetar spin-down model. Circle (black) is the optical component, diamond (red) is the NIR component, square (green) is the optical+NIR component, solid lines (black) are MAG1 and MAG2 (the lines overlap and cannot be distinguished), dot–dashed line (purple) is the fully-trapped magnetar spin-down fit from Chatzopoulos et al. (2012) implemented by TigerFit.

3.3.3 *Magnetar spin-down*

In this section, we fit the magnetar spin-down model to the light curve of SN 2008es. The model is (Kasen & Bildsten 2010; Woosley 2010; Chatzopoulos et al. 2012)

$$L(t) = \frac{2}{t_{LC}} \exp\left[-\frac{t^2}{t_{LC}^2}\right] \times \int_0^t \exp\left[\frac{t'^2}{t_{LC}^2}\right] \left(\frac{t'}{t_{LC}}\right) L_{mag}(t')\,dt', \quad (2)$$

$$L_{mag}(t) = \frac{E_p}{t_p}\left(1 + \frac{t}{t_p}\right)^{-2}; t > t_p, \quad (3)$$

where L is the observed luminosity at time t after the explosion powered by dipole-dominated magnetar spin-down with initial rotational energy E_p and initial spin-down time-scale t_p, passing through homologously expanding diffusive material with effective light-curve time-scale t_{LC} and small initial radius. Additionally, we apply the trapping function $T = (1 - \exp[-At^{-2}])$, where A is the trapping coefficient and $A \to \infty$ for fully trapped energy (Chatzopoulos et al. 2012, 2013; Wang et al. 2015, 2016; Dai et al. 2016). There are two different implementations for the trapping function, which we call case 'O' for being outside the integral and case 'I' for being inside the integral. Physically, case 'O' assumes that the bulk input luminosity is fully trapped during the diffusion process but the observed luminosity is not, while case 'I' assumes that the diffusion process cannot fully trap the input luminosity.

Table 6 and Fig. 6 present the best-fitting results by feeding only the early-time post-peak data; because of the condition $t > t_p$ as given in equation (3), we omit the pre-peak data, and because of the uncertainty of the later-time conditions (e.g. changes in opacity and hard photon leakage) that are invalid for the model assumptions, we also omit the later-time data. Additionally, we plot the solution from Chatzopoulos et al. (2013) as the case of fully trapped energy for comparison purposes. This solution greatly overpredicts the late-time brightness.

The solutions MAG1/MAG2, which differ in the implementation of the trapping function but yield insignificantly different results, have the effective light-curve time-scale ~19 d comparable to the spin-down time-scale ~24 d, and have initial rotational energy $\sim 10^{51}$ erg. By applying equations 1 and 2 of Kasen & Bildsten (2010) and equation 10 of Chatzopoulos et al. (2013), the typical solution implies a magnetar with initial spin period $P \approx 3$ ms, field strength $B \approx 10^{14}$ G, and ejecta mass $M_{ej} \approx 0.5\ M_\odot$.[4] This solution is consistent with the SLSN magnetar described by Metzger et al. (2015), and it is also consistent with results from other studies (Kasen & Bildsten 2010; Chatzopoulos et al. 2013; Inserra et al. 2018). The solution fits the early-time data well, but predicts a brighter later-time light curve than what is observed. At 255 d, the discrepancy between the prediction of the typical solution and the observation is $\sim 5 \times 10^{41}$ erg s^{-1}, given that the optical and NIR components are summed together. The discrepancy at late times is a common issue of fitting SLSNe with the magnetar model (Kasen & Bildsten 2010; Chatzopoulos et al. 2013; Wang et al. 2015; Inserra et al. 2018). X-ray leakage or ionization breakout is hypothesized to explain the discrepancy. However, besides SCP06F6 (SLSN I) showing very bright X-ray emission at early times (Levan et al. 2013) and weak X-ray emission from SN 2006gy (Smith et al. 2007), there have been no other detections from the X-ray observations (especially in SLSNe I; Margutti et al. 2018).

Thus, we do not favour the magnetar model because the fit to the late-time observations is poorer compared to the CSI models, and the magnetar scenario is likely incompatible with the observation of CDS dust, since the hot bubble produced by the magnetar is hostile to dust condensation (Metzger et al. 2014). However, we note that the magnetar scenario currently cannot be ruled out.

4 CONCLUSION

We present and analyse late-time data (192–554 d after explosion in the rest frame) for SN 2008es, including optical/NIR photometry and spectroscopy of H α. The spectra show prominent and broad H α emission without any detected narrow component. Red-wing attenuation is present as early as 288 d, implying strong CSI and dust formation in the CDS. The blue-wing side of the emission extends to about 10 000 km s^{-1}, similar to the earlier time data. The late-time photometry is consistent with a cooling SN photosphere and a NIR-excess component at $T \approx 1500$ K, implying thermal dust emission. The distance argument supports newly formed CDS dust being responsible for emitting the NIR excess, possibly heated by CSI.

[4]We note that in the literature, there are slightly different definitions for calculating the spin-down time-scale with different specifications. We follow the definition of Kasen & Bildsten (2010). See Nicholl, Guillochon & Berger (2017) for a discussion of different specifications.

The analysis of the light curve supports CSI as the main powering mechanism from early times until the observed later-time epochs. The fit to the CSI model yields $\sim$10–20 $M_\odot$ of ejecta and $\sim$2–3 $M_\odot$ of CSM with either a uniform or steady-wind distribution. For the uniform-distribution model, the density is $\sim 10^{-13}$–10^{-12} g cm^{-3}, while for the steady-wind model the mass-loss rate is $\sim$0.1–1 $M_\odot$ yr^{-1} for a wind velocity of $\sim$100 km s^{-1}, consistent with that of an LBV-like great eruption. A uniform-density CSM shell is more likely than a stellar-wind structure. The effective CSM radius is $\sim 10^{15}$ cm, supporting the efficient conversion of shock energy to radiation by CSI. Only a small amount of ^{56}Ni is allowed, $\lesssim$0.4 $M_\odot$ (if excluding CSI) or 0.04 $M_\odot$ (if including CSI). The CSI powering scenario also provides a consistent explanation for the CDS dust condensation and strong H α emission. The magnetar spin-down powering mechanism cannot be ruled out, but it is less favourable because of the large brightness discrepancy at late times. Moreover, it is not consistent with other evidence at late times such as the NIR excess from dust and strong CSI.

We note some limitations of our analysis. (1) The assumption of spherical symmetry of the CSM might not be valid, given the growing evidence supporting asymmetric or clumpy CSM (Chugai et al. 2005; Fox et al. 2009, 2010, 2011; Kotak et al. 2009; Andrews et al. 2010, 2011, 2016; Tinyanont et al. 2016). If this is the case, the interpretation of the condensation of the CDS dust will need to be reconsidered. However, this should not affect our other interpretations including the CDS dust condensation, which is still supported by the NIR excess and additional arguments. (2) The NIR observation is sensitive to warm dust, which corresponds to the CDS dust in our case. Colder dust located beyond the CDS could exist, and its emission might contaminate the NIR observation. If this were the case, we would overestimate the NIR contribution to the energy budget. However, this should not affect our interpretation of CDS dust. (3) The assumption of a blackbody might be invalid, especially at late times when line emission dominates in the nebular phase. This limitation can affect significantly the estimation of luminosity and temperature. (4) The diffusion approximation in both CSI and magnetar spin-down assumes spherical symmetry, homologous expansion, a centrally concentrated energy source, and constant opacity. Whether these assumptions hold for the analysis at late times is still unknown.

This work reveals, to some extent, the nature of SLSNe II lacking narrow features, a very rare class of which SN 2008es was the first object. We note two important aspects of the class that need to be studied: the powering mechanism and dust production. The powering mechanism tends to be explainable by efficient CSI better than by magnetar spin-down. However, whether SN 2008es is a good representative of the class or is a unique case is still unknown. More objects of a similar nature are required. Besides SN 2008es, SLSNe II without narrow features also include SN 2013hx and PS15br (Inserra et al. 2018). Investigating the late-time behaviour of these objects might shed some light on the subject, although this will be challenging since they are distant. X-ray and radio observations are recommended probes for the CSI, as observed in some SNe IIn (e.g. SN 1998S, Pooley et al. 2002; SN 2010jl, Chandra et al. 2015) and in superluminous SN 2006gy (Smith et al. 2007). To explore dust production, NIR to mid-IR observations are recommended probes for future objects, and should be attempted with the *James Webb Space Telescope*.

ACKNOWLEDGEMENTS

KB and RC acknowledge support from National Aeronautics and Space Administration (NASA) grant 80NSSC18K0665. Support for AVF's SN research has been provided by the NSF, the TABASGO Foundation, the Christopher R. Redlich Fund, and the Miller Institute for Basic Research in Science (U.C. Berkeley). AVF's work was conducted in part at the Aspen Center for Physics, which is supported by NSF grant PHY-1607611; he thanks the centre for its hospitality during the supermassive black holes workshop in 2018 June and July.

This study is based on observations obtained at the Gemini Observatory (Program ID GN-2009A-Q-48, PI Miller), which is operated by the Association of Universities for Research in Astronomy, Inc., under a cooperative agreement with the NSF on behalf of the Gemini partnership: the NSF (United States), the National Research Council (Canada), CONICYT (Chile), Ministerio de Ciencia, Tecnología e Innovación Productiva (Argentina), and Ministério da Ciência, Tecnologia e Inovação (Brazil).

Some of the data presented herein were obtained at the W. M. Keck Observatory, which is operated as a scientific partnership among the California Institute of Technology, the University of California, and NASA. The Observatory was made possible by the generous financial support of the W. M. Keck Foundation. We thank J. M. Silverman for assistance with some of the Keck observations and D. A. Perley for obtaining some of the Keck I/LRIS images. We thank M. Kasliwal for obtaining the P200/COSMIC images. Also, this research has made use of the KOA, which is operated by the W. M. Keck Observatory and the NASA Exoplanet Science Institute (NExScI), under contract with NASA. The authors wish to recognize and acknowledge the very significant cultural role and reverence that the summit of Maunakea has always had within the indigenous Hawaiian community. We are most fortunate to have the opportunity to conduct observations from this mountain.

REFERENCES

Aguilera-Dena D. R., Langer N., Moriya T. J., Schootemeijer A., 2018, ApJ, 858, 115
Andrews J. E. et al., 2010, ApJ, 715, 541
Andrews J. E. et al., 2011, AJ, 142, 45
Andrews J. E. et al., 2016, MNRAS, 457, 3241
Andrews J. E., Smith N., 2018, MNRAS, 477, 74
Andrews J. E., Smith N., McCully C., Fox O. D., Valenti S., Howell D. A., 2017, MNRAS, 471, 4047
Angus C. R., Levan A. J., Perley D. A., Tanvir N. R., Lyman J. D., Stanway E. R., Fruchter A. S., 2016, MNRAS, 458, 84
Arcavi I. et al., 2017, Nature, 551, 210
Aretxaga I., Benetti S., Terlevich R. J., Fabian A. C., Cappellaro E., Turatto M., della Valle M., 1999, MNRAS, 309, 343
Blanton M. R., Roweis S., 2007, AJ, 133, 734
Branch D., Wheeler J. C., 2017, Supernova Explosions, Springer-Verlag , Germany
Breeveld A. A., Landsman W., Holland S. T., Roming P., Kuin N. P. M., Page M. J., 2011, in McEnery J. E., Racusin J. L., Gehrels N., eds, AIP Conf. Proc. Vol. 1358. Am. Inst. Phys., New York, p. 373
Chandra P., Chevalier R. A., Chugai N., Fransson C., Soderberg A. M., 2015, ApJ, 810, 32
Chatzopoulos E., Wheeler J. C., Vinko J., 2012, ApJ, 746, 121
Chatzopoulos E., Wheeler J. C., Vinko J., Horvath Z. L., Nagy A., 2013, ApJ, 773, 76
Chevalier R. A., 1998, ApJ, 499, 810
Chevalier R. A., 2012, ApJ, 752, L2
Chevalier R. A., Fransson C., 2006, ApJ, 651, 381
Chevalier R. A., Fransson C., 2017, Thermal and Non-thermal Emission from Circumstellar Interaction, Springer International Publishing AG. p. 875
Chevalier R. A., Irwin C. M., 2011, ApJ, 729, L6

Chugai N. N., Fabrika S. N., Sholukhova O. N., Goranskij V. P., Abolmasov P. K., Vlasyuk V. V., 2005, Astron. Lett., 31, 792
Coppejans D. L. et al., 2018, ApJ, 856, 56
Curtis S., Ebinger K., Fröhlich C., Hempel M., Perego A., Liebendörfer M., Thielemann F.-K., 2019, ApJ, 870, 2
Dai Z. G., Wang S. Q., Wang J. S., Wang L. J., Yu Y. W., 2016, ApJ, 817, 132
Dexter J., Kasen D., 2013, ApJ, 772, 30
Dwek E., 1983, ApJ, 274, 175
Dwek E., 1985, ApJ, 297, 719
Elmhamdi A. et al., 2003, MNRAS, 338, 939
Faber S. M. et al., 2003, in Iye M., Moorwood A. F. M., eds, Proc. SPIE Conf. Ser. Vol. 4841, Instrument Design and Performance for Optical/Infrared Ground-based Telescopes. SPIE, Bellingham, p. 1657
Filippenko A. V., 1997, ARA&A, 35, 309
Fox O. et al., 2009, ApJ, 691, 650
Fox O. D. et al., 2011, ApJ, 741, 7
Fox O. D. et al., 2015, MNRAS, 454, 4366
Fox O. D., Chevalier R. A., Dwek E., Skrutskie M. F., Sugerman B. E. K., Leisenring J. M., 2010, ApJ, 725, 1768
Gal-Yam A. et al., 2009, Nature, 462, 624
Gal-Yam A., 2012, Science, 337, 927
Gall C. et al., 2014, Nature, 511, 326
Gall C., Hjorth J., Andersen A. C., 2011, A&AR, 19, 43
Gezari S. et al., 2009, ApJ, 690, 1313
Graham J., Meikle W., Evans A., Bode M., Albinson J., 1986, Light on Dark Matter. Springer, Netherlands, p. 397
Graham J. R. et al., 1983, Nature, 304, 709
Hamuy M., 2003, ApJ, 582, 905
Hanuschik R. W., Thimm G., Dachs J., 1988, MNRAS, 234, 41P
Hodapp K. W. et al., 2003, PASP, 115, 1388
Hook I. M., Jørgensen I., Allington-Smith J. R., Davies R. L., Metcalfe N., Murowinski R. G., Crampton D., 2004, PASP, 116, 425
Inserra C. et al., 2018, MNRAS, 475, 1046
Kasen D., Bildsten L., 2010, ApJ, 717, 245
Kotak R. et al., 2009, ApJ, 704, 306
Leitherer C. et al., 1999, ApJS, 123, 3
Leitherer C., Ortiz Otálvaro P. A., Bresolin F., Kudritzki R.-P., Lo Faro B., Pauldrach A. W. A., Pettini M., Rix S. A., 2010, ApJS, 189, 309
Leitherer C., Ekström S., Meynet G., Schaerer D., Agienko K. B., Levesque E. M., 2014, ApJS, 212, 14
Levan A. J., Read A. M., Metzger B. D., Wheatley P. J., Tanvir N. R., 2013, ApJ, 771, 136
Margutti R. et al., 2018, ApJ, 864, 45
Mauerhan J., Smith N., 2012, MNRAS, 424, 2659
Metzger B. D., Vurm I., Hascoët R., Beloborodov A. M., 2014, MNRAS, 437, 703
Metzger B. D., Margalit B., Kasen D., Quataert E., 2015, MNRAS, 454, 3311
Miller A. A. et al., 2009, ApJ, 690, 1303
Miller A. A., Smith N., Li W., Bloom J. S., Chornock R., Filippenko A. V., Prochaska J. X., 2010, AJ, 139, 2218
Moriya T. J., Tominaga N., 2012, ApJ, 747, 118
Nicholl M., Guillochon J., Berger E., 2017, ApJ, 850, 55
Ofek E. O. et al., 2007, ApJ, 659, L13
Oke J. B. et al., 1995, PASP, 107, 375
Oke J. B., Gunn J. E., 1983, ApJ, 266, 713
Pooley D. et al., 2002, ApJ, 572, 932
Pozzo M., Meikle W. P. S., Fassia A., Geballe T., Lundqvist P., Chugai N. N., Sollerman J., 2004, MNRAS, 352, 457
Rockosi C. et al., 2010, Proc. SPIE, 7735, 77350R
Schlafly E. F., Finkbeiner D. P., 2011, ApJ, 737, 103
Schulze S. et al., 2018, MNRAS, 473, 1258
Shiode J. H., Quataert E., 2014, ApJ, 780, 96
Smartt S. J., 2009, ARA&A, 47, 63
Smith N. et al., 2007, ApJ, 666, 1116
Smith N. et al., 2008c, ApJ, 686, 485
Smith N. et al., 2009b, ApJ, 695, 1334
Smith N. et al., 2015, MNRAS, 449, 1876
Smith N., 2006, ApJ, 644, 1151
Smith N., 2014, ARA&A, 52, 487
Smith N., 2017, Handbook of Supernovae. Springer International Publishing AG, p. 403
Smith N., Arnett W. D., 2014, ApJ, 785, 82
Smith N., Hartigan P., 2006, ApJ, 638, 1045
Smith N., McCray R., 2007, ApJ, 671, L17
Smith N., Owocki S. P., 2006, ApJ, 645, L45
Smith N., Gehrz R. D., Hinz P. M., Hoffmann W. F., Hora J. L., Mamajek E. E., Meyer M. R., 2003, AJ, 125, 1458
Smith N., Foley R. J., Filippenko A. V., 2008a, ApJ, 680, 568
Smith N., Chornock R., Li W., Ganeshalingam M., Silverman J. M., Foley R. J., Filippenko A. V., Barth A. J., 2008b, ApJ, 686, 467
Smith N., Hinkle K. H., Ryde N., 2009a, AJ, 137, 3558
Smith N., Chornock R., Silverman J. M., Filippenko A. V., Foley R. J., 2010, ApJ, 709, 856
Smith N., Silverman J. M., Filippenko A. V., Cooper M. C., Matheson T., Bian F., Weiner B. J., Comerford J. M., 2012, AJ, 143, 17
Soderberg A. M. et al., 2012, ApJ, 752, 78
Stathakis R. A., Sadler E. M., 1991, MNRAS, 250, 786
Stetson P. B., 1987, PASP, 99, 191
Stritzinger M. et al., 2012, ApJ, 756, 173
Suwa Y., Tominaga N., Maeda K., 2019, MNRAS, 483, 3607
Takahashi K., Yoshida T., Umeda H., Sumiyoshi K., Yamada S., 2016, MNRAS, 456, 1320
Tinyanont S. et al., 2016, ApJ, 833, 231
Tokunaga A. T., Vacca W. D., 2005, PASP, 117, 421
Turatto M., Cappellaro E., Danziger I. J., Benetti S., Gouiffes C., della Valle M., 1993, MNRAS, 262, 128
Vázquez G. A., Leitherer C., 2005, ApJ, 621, 695
, in Vink J. S., Vink J. S., 2015, ed., Very Massive Stars in the Local Universe, Astrophysics and Space Science Library Vol. 412. Springer International Publishing , Switzerland, p. 77
Wang L.-J., Wang S. Q., Dai Z. G., Xu D., Han Y.-H., Wu X. F., Wei J.-Y., 2016, ApJ, 821, 22
Wang S. Q., Wang L. J., Dai Z. G., Wu X. F., 2015, ApJ, 799, 107
Wheeler J. C., Chatzopoulos E., Vinkó J., Tuminello R., 2017, ApJ, 851, L14
Woosley S., Janka T., 2005, NatPh, 1, 147
Woosley S. E., 2010, ApJ, 719, L204
Woosley S. E., Blinnikov S., Heger A., 2007, Nature, 450, 390

This paper has been typeset from a TEX/LATEX file prepared by the author.